nature energy

ARTICLES

https://doi.org/10.1038/s41560-018-0237-6

Langmuir–Blodgett artificial solid-electrolyte interphases for practical lithium metal batteries

Mun Sek Kim[1], Ji-Hyun Ryu[1,2], Deepika[3], Young Rok Lim[1,4], In Wook Nah[1], Kwang-Ryeol Lee[3], Lynden A. Archer[5]* and Won Il Cho[1]*

Practical lithium metal batteries require full and reversible utilization of thin metallic Li anodes. This introduces a fundamental challenge concerning how to create solid-electrolyte interphases (SEIs) that are able to regulate interfacial transport and protect the reactive metal, without adding appreciably to the cell mass. Here, we report on physicochemical characteristics of Langmuir–Blodgett artificial SEIs (LBASEIs) created using phosphate-functionalized reduced graphene oxides. We find that LBASEIs not only meet the challenges of stabilizing the Li anode, but can be facilely assembled in a simple, scalable process. The LBASEI derives its effectiveness primarily from its ability to form a durable coating on Li that regulates electromigration at the anode/electrolyte interface. In a first step towards practical cells in which the anode and cathode capacities are matched, we report that it is possible to achieve stable operations in both coin and pouch cells composed of a thin Li anode with the LBASEI and a high-loading intercalation cathode.

High-performance rechargeable batteries with new and efficient chemistries able to outperform state-of-the-art lithium ion battery (LiB) technology are particularly needed. In addition to meeting device storage and portability requirements, a successful rechargeable battery must also satisfy many other demands, including life time, safety and cost[1]. Meeting all of these demands in a closed electrochemical cell that in some cases must operate trouble-free for hundreds of cycles and thousands of hours is a formidable challenge because it requires high levels of reversibility in all components of the cell[2–5]. Key to success in achieving such levels of reversibility is the control of the composition, structure, mechanics and transport properties of the few-nanometre interfacial materials' phases (interphases) that form spontaneously near the highly reducing anode, as well as near the increasingly oxidizing cathodes of contemporary interest[6–13].

The benefits of replacing the graphitic carbon anode of the LiB with metallic Li have been thoroughly reviewed in the recent literature[2,10,14]. The potential for substantial improvements in storage capacity per unit volume and mass afforded by this change are among the most important drivers of interest in Li metal anodes. Rechargeable batteries based on Li metal anodes are also advantageous because they provide greater freedom to choose cathodes that are themselves unlithiated materials (for example, S_8 and O_2). However, fundamental challenges associated with the high chemical reactivity of Li, the poor quality of the heterogeneous interphases Li forms spontaneously in contact with all electrolytes and difficulty controlling the morphology of Li electrodeposits during battery recharge have so far presented formidable barriers to progress in achieving practical rechargeable batteries based on the Li anode[11]. Among the various approaches, rationally designed artificial solid-electrolyte interphases (ASEIs) on Li show greatest promise for their potential to address physicochemical instabilities responsible for the poor reversibility of the Li anode[7,8,13,15,16].

Here, we report that a continuous Langmuir–Blodgett process termed Langmuir–Blodgett scooping (LBS) facilitates straightforward and scalable creation of robust Langmuir–Blodgett ASEIs (LBASEIs) composed of functionalized and doped graphene materials with well-defined thicknesses on Li metal (LiM) anodes. In particular, it is shown that uniform LBASEI coatings deposited on a non-reactive substrate in aqueous media can be facilely transferred to the LiM via a roll-press process. LBASEIs based on graphene with diverse functional groups, including phosphates, phosphorus and nitrogen, are observed to interact strongly with Li, simultaneously protecting the LiM anode from parasitic reactions with liquid electrolytes and enabling flat, two-dimensional, Li electrodeposition. Building on these findings, we design electrochemical cells in which the LBASEI on the Li anode (LBASEI Li) is paired with commercial, high-loading Li nickel cobalt manganese oxide (NCM) cathodes in coin- and pouch-cell configurations and show that it is possible to achieve highly reversible and stable cell operations. Significantly, we find that even in cells in which a thin Li layer (20 μm thick) is used as the anode to produce batteries in which the anode and cathode capacities are matched, stable cycling is achieved for >200 cycles. To understand the source of these performance benefits, we use a combination of surface analytical and computational analysis to show that the LBASEI based on phosphate-functionalized reduced graphene oxide facilitates nucleation of Li electrodeposits and thereby enables uniform migration of Li at the interface between the liquid electrolyte and a planar solid surface that is selectively permeable to Li ions in the electrolyte.

Langmuir–Blodgett artificial solid-electrolyte interphases

Among the most important requirements of successful ASEIs for the LiM anode are the ability to provide stable nucleation sites for Li deposition, fast interfacial transport of Li ions and a quasi-hosting feature for Li that protects the freshly deposited Li from exposure to reactive electrolytes[16–19]. Graphene is an attractive choice for the

[1]Center for Energy Storage Research, Korea Institute of Science and Technology, Seoul, Republic of Korea. [2]Department of Materials Science and Engineering, Korea University, Seoul, Republic of Korea. [3]Center for Computational Science Research, Korea Institute of Science and Technology, Seoul, Republic of Korea. [4]Department of Chemistry, Korea University, Sejong, Republic of Korea. [5]School of Chemical and Biomolecular Engineering, Cornell University, Ithaca, NY, USA. *e-mail: laa25@cornell.edu; wonic@kist.re.kr

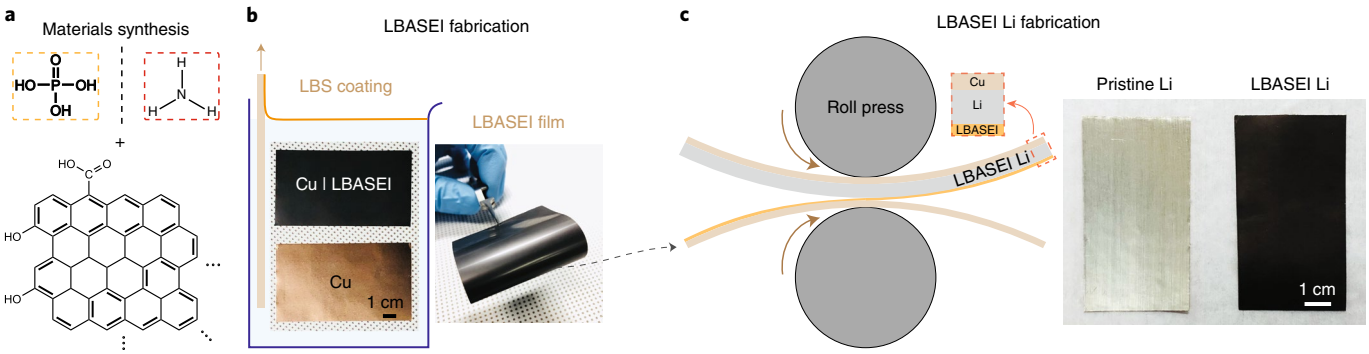

Fig. 1 | LBASEI designs and fabrication processes for the LBASEI Li electrode. a, Two types of graphene oxide are considered: PrGO and NrGO. Molecular structures of the phosphoric acid and ammonia gas precursors are illustrated, and the resultant PrGO and NrGO are produced by the provided synthesis. **b**, LBASEI fabrication process via the LBS method. The inset images show the substrate (Cu), LBASEI-coated Cu (Cu|LBASEI) and mechanical stability of the substrate-coated LBASEI. **c**, Fabrication of the LBASEI Li via a roll-press process. Briefly, the Cu|LBASEI is sandwiched with the LiM and uniformly pressed with evenly distanced cylinders to transfer the LBASEI from the LBASEI|Cu to the exposed surface of the Li. The inset pictures are images taken before (pristine Li) and after (LBASEI Li) the LBASEI transfer.

ASEI for the LiM anode because of its high electronic conductivity and facilitated diffusion of Li ion on surfaces and within interlayer gaps[16,17,20–22]. To illustrate the role of the surface chemistry of the ASEI, phosphate-functionalized reduced graphene oxide (PrGO) is investigated for its ability to strongly bind the Li, and is compared with nitrogen-doped reduced graphene oxide (NrGO). Two synthesis procedures are used to create the modified graphene oxides: pyrolyzing reduced graphene oxide (rGO) with phosphoric acid under an inert environment to derive PrGO and reducing graphene oxide under ammonia gas atmosphere to obtain NrGO (Fig. 1a). An advantage of the method reported here for coating the functionalized graphene oxides on LiM is that while facilitating nanoscale thickness control of the ASEI on the LiM electrode, it also offers simplicity and scalability. Specifically, ASEIs produced by other approaches require pre-deposition of Li (refs [16–18,22,23]) or infusion of molten Li (refs [24–26]) to utilize the ASEI and quasi-host for the LiM anode. However, the requirement for pre-deposited Li is problematic as the Li deposition is often non-uniform for large dimensions and cumbersome for full-cell fabrications. Also, infusion of molten Li requires free-standing substrates that are relatively thick and heavy, which is not desirable for practical lithium metal batteries (LiMBs).

Recently, Chen and co-workers[27] utilized a conventional Langmuir–Blodgett trough technique to create a graphene ASEI on a $LiMn_2O_4$ cathode to suppress Jahn–Teller distortion of the cathode and to alleviate oxidation of the secondary conductor carbon in the cathode for aqueous lithium batteries. The major technical differences between the conventional LB trough approach and the LBS method reported here lie with the film formation mechanism[28]. Specifically, whereas the LB trough method relies on mechanical compression of a buoyant film deposited at an air/water interface to create ordered surface coatings, the LBS method takes advantage of the Marangoni effect to spontaneously form highly ordered coatings at the air/water interface. This difference is significant as it replaces the discontinuous and slow LB trough approach with a continuous process that can be used to facilely create nanoparticulate films on water-stable substrates. These features enable rapid and precise coatings on the solid substrate in a scalable manner[28,29]. As shown in Fig. 1b, LBASEIs can be fabricated under ambient conditions on a wide range of water-stable substrates to produce compact and uniform nanoparticulate films with controlled thicknesses. Supplementary Video 1 shows that the process is scalable and can be adapted for large-scale preparation of the LBASEIs. The ordered packing of the graphene oxide materials induced by the Marangoni effect during the deposition process provides enhanced adhesion among the particles due to closed-packing, and LBS's binder-free deposition allows facile detachment of the LBASEI at a substrate/LBASEI interface. The softness of the LiM surface facilitates transfer of the LBASEI onto the LiM without a need of adhesives via the roll-press process, as illustrated in Fig. 1c and Supplementary Video 2.

Lithium nucleation and adsorption sites on the LBASEI

The surface characteristics of three different graphene oxides (rGO, NrGO and PrGO) were analysed via X-ray photoelectron spectroscopy (XPS) analysis (Fig. 2a). Key differences are observed among the graphene oxides, including the existence of P 2*p* (Fig. 2b) and N 1*s* (Fig. 2c) peaks for PrGO and NrGO. For PrGO, deconvolution of P 2*p* peak at 135 eV verifies the presence of pyrophosphate (P_2O_7) and metaphosphate (P_3O_9) with binding energies of 134.2 and 135.1 eV, respectively. The N 1*s* peak for NrGO shows the presence of pyrrolic (N_{pr}), pyridinic (N_{pd}) and quaternary (N_q) N with binding energies of 399.3, 397.8 and 401.1 eV, respectively. To quantitatively understand the interaction of a Li atom with various species, binding energy and two-dimensional local charge density profiles are analysed based on density functional theory calculations using the Vienna Ab-initio Simulation Package (VASP)[30].

Figure 2d shows the binding energies of the Li atom for the following species: graphene (G), −0.579 eV; P_2O_7, −2.514 eV; P_3O_9, −2.443 eV; bulk phosphorus (P), −1.464 eV; N_{pr}, −1.379 eV; N_{pd}, −1.003 eV; and N_q, −0.183 eV. Their corresponding molecular structures are shown in Fig. 2e. The P_2O_7 and P_3O_9 on PrGO exhibit relatively high binding energies compared with the other species. It is apparent that the functional groups present in PrGO have better binding energies than all the nitrogen species in NrGO. We hypothesize that the strong interactions of especially phosphate functional groups in PrGO with the Li should lead to enhanced Li adsorption and nucleation, which should in turn promote planar and more compact electrodeposition of Li, making PrGO a preferred LBASEI compared to NrGO and rGO LBASEIs. Figure 2f shows two-dimensional local charge density profiles along with a projection of charge densities, in which the binding locations favourable for the Li adsorption sites on G, P, P_2O_7 and P_3O_9 structures are evident. For graphene, it is favoured for Li to be adsorbed at the centre of the honeycomb located near the edges. In the case of P substituted in the graphene, Li is likely to adsorb on the top of P due to the presence of one extra electron and a relatively bigger atomic radius of P than C. This results in an increase in the C–P bond and thus favours out-of-plane physical interactions between the Li and P atoms. For the functional groups in PrGO, oxygen groups available

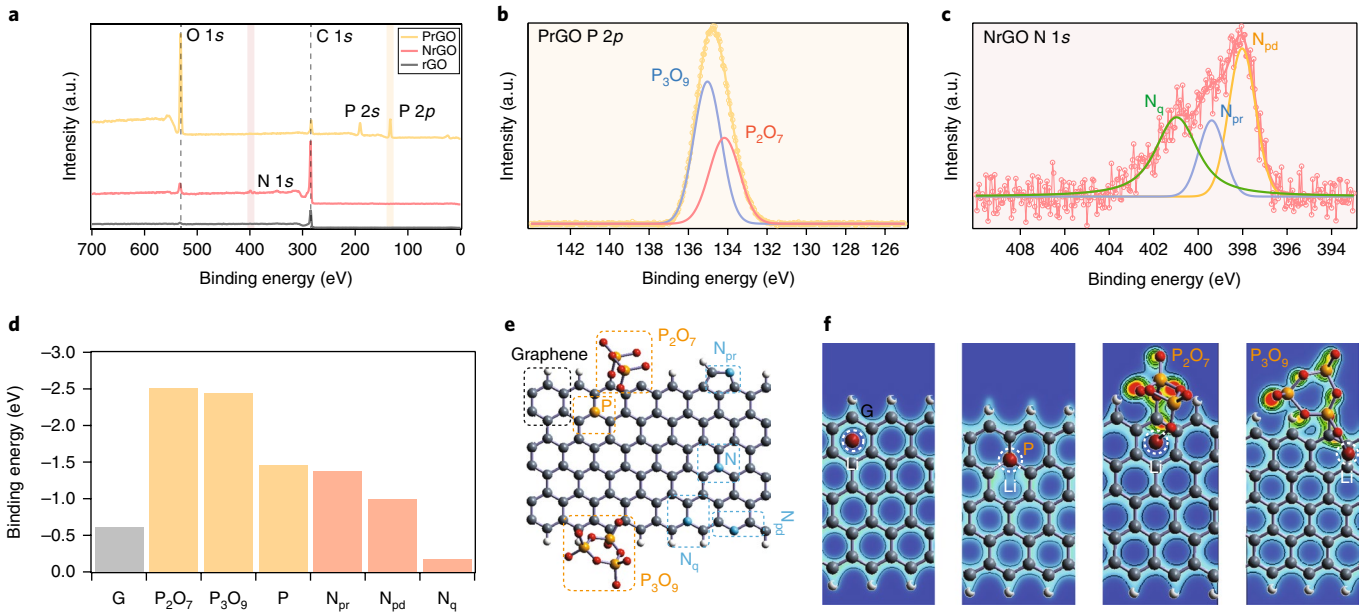

Fig. 2 | Interactive sites of the lithium on the LBASEI. a, XPS spectrum of PrGO, NrGO and rGO. The dashed grey lines indicate the common O 1s and C 1s peaks present for all three samples. The orange and red regions represent distinctive binding peaks present for PrGO and NrGO, respectively. **b**, P 2*p* XPS spectrum of PrGO. The empty orange circles and orange line represent the raw and fitted data, respectively. The orange line fitting was done via Origin Pro using a Gaussian peak type. The blue and red lines represent deconvoluted peaks for P_3O_9 and P_2O_7 bindings. **c**, N 1s XPS spectrum of NrGO. The empty red circles and red line represent the raw and fitted data, and green, blue and orange lines represent deconvoluted peaks for N_q, N_{pr} and N_{pd} bindings, respectively. The red line fitting was done via Origin Pro using a Gaussian peak type. **d**, Binding energies of the Li atom with graphene (G), P_2O_7, P_3O_9, bulk phosphorus (P), N_{pr}, N_{pd} and N_q species. **e**, Molecular structures of the species in **d** and bulk nitrogen (N). **f**, Projected charge densities after Li atom adsorption on G, P, P_2O_7 and P_3O_9. Charge density is plotted along the (001) plane. Grey, white, maroon, red and gold spheres represent carbon, hydrogen, lithium, oxygen and phosphorus atoms, respectively. The red region corresponds to higher charge density in reference to the blue region. The adsorbed Li (maroon atom) on the presented structures is identified by the white dashed circles. Note that the P (gold atom) is beneath the adsorbed Li atom in the charge density of P.

in P_2O_7 and P_3O_9 serve as favourable sites for the adsorption of Li atoms due to the presence of a free electron pair on oxygen. The free electron pair forms a localized and uniform charge cloud around the P_2O_7 and P_3O_9, due to the symmetric nature of P_2O_7 and P_3O_9, that strongly attracts the electron-deficient Li ion in an electrolyte. Thus, strong and uniform binding of the Li is achieved with P_2O_7 and P_3O_9 compared with other available species. In Supplementary Fig. 1, the projected charge densities for the species in NrGO are shown, where the trend of the binding is in agreement with a previous report[22]. N_{pr} and N_{pd} are likely to interact strongly with Li whereas Li prefers G over N_q and N, which means that not all nitrogen species in NrGO enhance strong bindings of Li over the G. These results validate our hypothesis and provide a design principle for constructing LBASEIs for the LiM anode.

As PrGO consists of functional groups that strongly interact with the Li, the Li nucleation overpotential of a PrGO LBASEI is measured and compared with that of rGO and NrGO LBASEIs. Figure 3a shows galvanostatic nucleation overpotential voltage profiles of asymmetric Li cells, with electrode configurations of Cu|Li, Cu/rGO|rGO/Li, Cu/NrGO|NrGO/Li and Cu/PrGO|PrGO/Li, measured at a fixed current density of 0.05 mA cm^{-2}. As graphene intercalates the Li, Li plating is thought to follow saturation of the graphene with the Li, explaining the potential excursion below 0 V. Although Cu is less likely to react or form an alloy with the Li at ambient conditions, an intrinsic SEI formation on the electrodes' interfaces at the beginning of a redox reaction consumes the Li and electrolyte with an amount of 0.007 mAh cm^{-2}. The rGO, NrGO and PrGO show Li intercalation capacities of 0.067, 0.092 and 0.123 mAh cm^{-2}, respectively, which include the materials' capacity as well as the intrinsic SEI formations on the electrodes. The capacity differences among the graphene oxides arise from different densities of the deposited LBASEI on the substrate due to particle morphology variations (Supplementary Fig. 2). Refer to Supplementary Note 1 for an analysis of the nucleation overpotential voltage profiles. The nucleation overpotentials (μ_{nuc}) are calculated by taking differences between a tip potential (μ_{tip}) and a mass-transfer controlled potential (μ_{mtc}). Calculated μ_{nuc} values for Cu (34.3 mV), rGO (23.7 mV), NrGO (21.1 mV) and PrGO (19.7 mV) are shown in Fig. 3b. Consistent with the trend in binding energies shown in Fig. 2d, PrGO is seen to have the lowest μ_{nuc}. In Supplementary Fig. 3, Li electrodeposits on PrGO LBASEI are compared with those on NrGO and rGO LBASEIs, where the Li electrodeposits are the smoothest for the PrGO LBASEI. Figure 3c shows the voltage profiles of the PrGO LBASEI for thicknesses ranging from 0 to ~3.01 µm. The μ_{nuc} values of the PrGO LBASEI based on thicknesses ranging from 0 to ~3.01 µm are 34.3, 25.8, 21.7, 20.1, 19.8, 18.1, 17.0 and 16.8 mV (see Fig. 3d). Importantly, the μ_{nuc} tends to remain steady for LBASEI thicknesses above ~2 µm, providing a convenient approach for optimizing the LBASEI thickness (Supplementary Note 2).

Overall, the Li migration process on the LBASEI can be summarized as in Fig. 3e. Based on the theoretical and experimental results, we came to the conclusion that PrGO is a suitable material for constructing the LBASEI due to its stable Li migration properties. Also, the thickness, one of the crucial factors for designing LBASEIs, is optimized and set to 2–3 µm for actual application in LiMBs. Utilizing a thin LBASEI is highly applicable for thin LiM anodes, which are required to construct reliable LiMBs. As the LiMB community is shifting to utilize thin LiM anodes (<30 µm, which has a capacity of ~6.2 mAh cm^{-2})[1], ultrathin (<5 µm) and

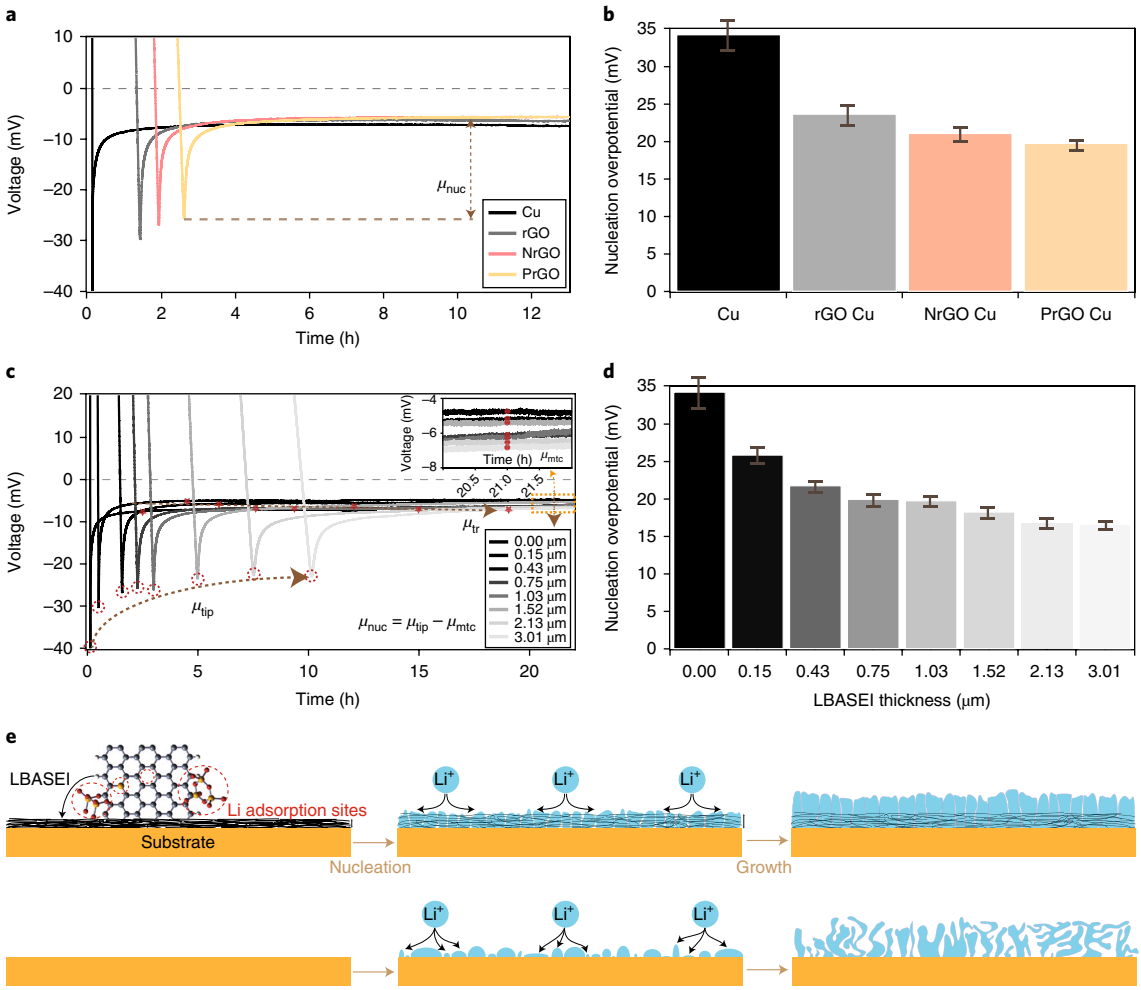

Fig. 3 | Lithium nucleation overpotential analysis for the LBASEIs. a, Galvanostatic Li electrodeposition voltage profiles for asymmetric Li cells (Cu|Li, Cu/rGO|rGO/Li, Cu/NrGO|NrGO/Li and Cu/PrGO|PrGO/Li) measured at a fixed current density of 0.05 mA cm^{-2}. The thicknesses of rGO, NrGO and PrGO are ~1 µm. **b**, Li nucleation overpotentials measured at the fixed current density of 0.05 mA cm^{-2} for the Cu, rGO Cu, NrGO Cu and PrGO Cu substrates. Three identical cases of each conditioned cell were measured and averaged to obtain the error bars. The standard error bar details for substrate types are specified accordingly: sample size of 3 for the each type, mean and standard deviations of 34.31 mV and 1.85 mV for Cu, 23.71 mV and 1.05 mV for rGO, 20.82 mV and 1.08 mV for NrGO, and 19.79 mV and 0.61 mV for PrGO. **c**, Galvanostatic Li deposition voltage profiles for the range of PrGO LBASEI thicknesses measured at the fixed current density of 0.05 mA cm^{-2}. μ_{tip}, μ_{mtc} and μ_{tr} are indicated with dashed red circles, filled red circles in the inset and filled red stars, respectively. **d**, Li nucleation overpotentials measured at the fixed current density of 0.05 mA cm^{-2} for PrGO LBASEI thicknesses ranging from 0 to ~3.01 µm. Three identical cases of each conditioned cells were measured and averaged to obtain the error bars. The standard error bar details for substrate types are specified accordingly: sample size of 3 for each condition, mean and standard deviations of 34.31 mV and 1.85 mV for 0 µm, 25.9 mV and 0.98 mV for 0.15 µm, 21.8 mV and 0.66 mV for 0.43 µm, 20.03 mV and 0.62 mV for 0.75 µm, 19.79 mV and 0.61 mV for 1.03 µm, 18.29 mV and 0.56 mV for 1.52 µm, 16.69 mV and 0.73 mV for 2.13 µm, and 16.90 mV and 0.24 mV for 3.01 µm. **e**, Schematic of the LBASEI design with the Li nucleation and growth processes with and without the LBASEI. The illustration depicts that the phosphate functional groups present in the LBASEI help Li to stably nucleate initially and uniformly grow the Li nuclei via interlayer gaps of and above and under the LBASEI. However, without the LBASEI, random nucleation of the Li is introduced and leads to uneven growth of the Li nuclei which eventually forms dendritic Li dendrites.

lightweight ASEIs are inevitable to construct pragmatic LiMBs. The promising features of carbon-based quasi-hosts, light yet heavier than Li, for the LiM anode have been studied recently[10,14,17,18]; however, these often hinder decreasing the carbon content of the actual LiM anode. To make a practical 20 µm LiM anode with any ASEI, >70 wt% and >80 vol% of the Li content in the anode is favoured as these specifications allow the LiMBs to overcome volumetric/gravimetric energy densities of LiBs. For the reasons above, the LBASEI thicknesses between 2 and 3 µm are adequate, which is discussed later, and ultimately paired with the 20 µm LiM anode (Li weight and volume contents of ~75% and ~89%, respectively, for LBASEI Li anode) to investigate the electrochemical performance of the LBASEI Li anode in full-cell batteries.

Lithium migration properties of the LBASEI

Li migration onto the LBASEI is further investigated using asymmetric and symmetric Li cells. Figure 4a shows the results from scanning electron microscope (SEM) analysis of the LBASEI-coated Cu (Cu|LBASEI) and the LBASEI correspondingly transferred onto the LiM (Li|LBASEI), and the insets show actual images of the fabricated Cu|LBASEI and Li|LBASEI electrodes. These electrodes are paired to make asymmetric Li cells with electrode configurations designated as Cu|Li for the reference cell and Cu/LBASEI|LBASEI/Li for the modified cell, which can be used to quantify the coulombic efficiency (CE) of the cells (see Fig. 4b). The asymmetric cell is used here to understand the relative efficiency of Li migration onto the LBASEI Li, compared with pristine Li. High Li reversibility and CE

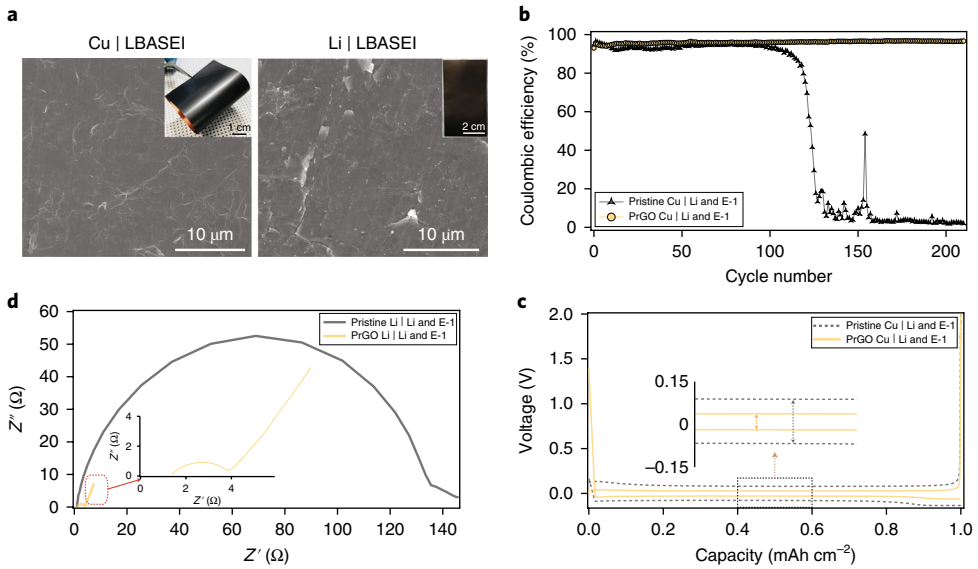

Fig. 4 | Electrochemical properties of the LBASEI. a, SEM images of the LBASEI on Cu (Cu|LBASEI) and LBASEI on Li (Li|LBASEI). The insets show actual images of the fabricated Cu|LBASEI and Li|LBASEI electrodes. **b**, CE as a function of cycle number for pristine Cu|Li and PrGO Cu|Li asymmetric cells with E-1 electrolyte. **c**, Corresponding voltage profiles of **b** for the pristine Cu|Li and PrGO Cu|Li asymmetric cells at the 100th cycle. The inset voltage profiles show the Li migration μ_{mtc} from 0.4 to 0.6 mAh cm^{-2} for the PrGO Cu|Li (solid orange) and the pristine Cu|Li (dahsed grey) asymmetric cells, and the orange and grey dashed arrows indicate a degree of the Li migration potentials of the μ_{mtc} for the PrGO Cu|Li and the pristine Cu|Li asymmetric cells. **d**, Nyquist plots for the uncycled pristine Li|Li and PrGO Li|Li symmetric cells with E-1 electrolyte. In the Nyquist plots, an imaginary part (−*Z*'') and a real part (*Z*') of characterisitc curves are plotted as *y* axis and *x* axis.

(~99%) are achieved for the LBASEI electrodes, Cu/PrGO|PrGO/Li (PrGO Cu|Li), at a current density of 1 mA cm^{-2} and capacity of 1 mAh cm^{-2} (approximately 4.85 μm of the Li passed per cycle, assuming a flat deposition). The pristine Cu|Li cell fails after about the 100th cycle, but the PrGO Cu|Li cell evidently exhibits a much longer cycle life. The low Li migration μ_{mtc} at the 100th cycle, as revealed by the galvanostatic voltage profiles in Fig. 4c, explains the stable Li migration onto the LBASEI by means of SEI preservations. The CE values recorded for the PrGO Cu|Li cell at higher current density and capacity of 3 mA cm^{-2} and 3 mAh cm^{-2} are reported in Supplementary Fig. 4. Electroplated Li morphologies on PrGO Cu, PrGO Li, pristine Cu and pristine Li are shown in Supplementary Fig. 5, and PrGO Cu and PrGO Li evidently show more uniform electrodeposits of Li than that on pristine Cu and pristine Li. a.c. impedance spectroscopy was conducted to observe the interfacial impedance of the LBASEI Li and pristine Li. In Fig. 4d, much smaller interfacial impedance (~2.7 Ω) is obtained for the LBASEI Li symmetric cell than for the pristine Li symmetric cell (~140 Ω) at an uncycled condition. Furthermore, the interfacial impedances are also measured after cycling the LBASEI Li and the pristine Li symmetric cells (Supplementary Fig. 6). See Supplementary Note 3 for detailed explanations about the impedance evolution. To investigate the reversibility of the Li migration onto the LBASEI Li, symmetric cells of Li/PrGO|PrGO/Li (PrGO Li|Li) and Li|Li (pristine Li|Li) were prepared and cycled at 1 mA cm^{-2} and 1 mAh cm^{-2} (Fig. 5a). Magnified voltage profiles in Fig. 5a for cycle numbers 0 to 10 and 220 to 230 are provided in Fig. 5b,c. In agreement with the impedance results, lower μ_{mtc} values as well as better potential retentions are achieved for the LBASEI Li than for the pristine Li. While the μ_{mtc} overshoots, implicating high interfacial impedance, for the pristine Li symmetric cell after the 210th cycle, the LBASEI Li symmetric cell maintains its μ_{mtc} for more than 400 cycles, which is equivalent to >800 h. The SEM images of the cycled pristine Li (Fig. 5d) and the LBASEI Li (Fig. 5e) electrodes further support the claim. The cycled pristine Li electrode shows a rough and porous surface whereas the cycled LBASEI Li electrode exhibits dense and smooth surface morphologies.

The CE associated with Li migration measurements at an inert counterelectrode is a commonly used approach for evaluating electrochemical stability of the interfaces Li forms with electrolytes[31]. However, a drawback of this approach is that these measurements are taken at a relatively low potential where few rechargeable batteries operate. This means that the levels of improvements one might deduce for conventional Li migration experiments in the asymmetric cells may not directly correlate with actual performances of cells and batteries. The different operating voltage windows, especially potentials above 3.5 V, and various cathode materials largely affect interfacial properties of the electrodes in cells. In addition, the electrochemical performance of the cells varies as the electrolyte decomposition differs based on working potentials of the cells, thus SEI evolutions on the electrodes vary and are sensitive to redox potentials defined by the cell chemistries. To justify this argument, different electrolytes E-1 and E-2 were chosen and the Li CE and Li migration measurements were performed with both asymmetric and symmetric cells. Accordingly, support for this observation is provided in Supplementary Fig. 7 where although the LBASEI Li asymmetric cell exhibits better performance than that of the pristine Li asymmetric cell, the absolute performance of the cells with E-2 electrolyte is worse than that with E-1 electrolyte. Furthermore, the Li migrations for the symmetric cells of the PrGO Li|Li and the pristine Li|Li are measured at 1 mA cm^{-2} and 1 mAh cm^{-2} with E-2 electrolyte (Fig. 5f). Magnified voltage profiles in Fig. 5f for cycle numbers 0 to 10 and 220 to 230 are provided in Fig. 5g,h. Lower Li μ_{mtc} values and better retention rates are achieved for the LBASEI Li symmetric cell than for the pristine Li symmetric cell. However, the overall results with E-2 electrolyte are actually worse than in the case of using E-1 electrolyte. Also, different morphologies of the cycled electrodes, compared with the electrodes using E-1 electrolyte, for both the LBASEI Li and pristine Li are observed for the cells using E-2 electrolyte. Denser, rigid and rod-like dendrites are observed

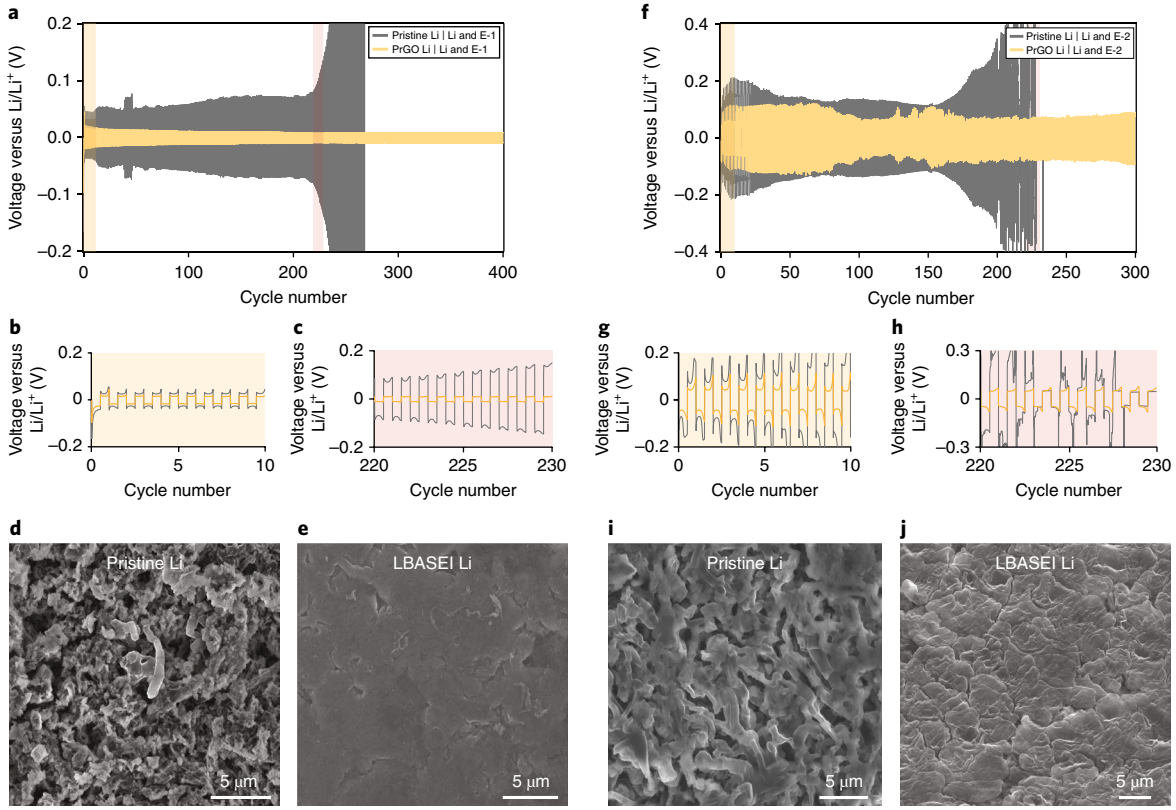

Fig. 5 | Li migration properties of the LBASEI. a, Galvanostatic Li plating/stripping voltage profiles for the pristine Li|Li and PrGO Li|Li symmetric cells at a fixed current density of 1 mA cm^{-2} and capacity of 1 mAh cm^{-2} with E-1 electrolyte. **b**,**c**, Magnified voltage profiles from 0th to 10th (**b**) and 220th to 230th (**c**) cycles as indicated by the orange and red regions in **a**, respectively. **d**,**e**, Surface morphology of the pristine Li (**d**) and the LBASEI Li (**e**) electrodes after the 100th galvanostatic Li stripping/plating cycle with E-1 electrolyte. **f**, Galvanostatic Li plating/stripping voltage profiles for the pristine Li|Li and PrGO Li|Li symmetric cells at the fixed current density of 1 mA cm^{-2} and capacity of 1 mAh cm^{-2} with E-2 electrolyte. **g**,**h**, Magnified voltage profiles from 0th to 10th (**g**) and 220th to 230th (**h**) cycles as indicated by the orange and red regions in **f**, respectively. **i**,**j**, Surface morphology of the pristine Li (**i**) and LBASEI Li (**j**) electrodes after the 100th galvanostatic Li stripping/plating cycle with E-2 electrolyte.

for the pristine Li (Fig. 5i) electrode, and expanded and dense graphene flake-like morphologies are shown for the LBASEI Li (Fig. 5j) electrode with E-2 electrolyte, whereas more porous morphologies of the electrodes are observed with E-1 electrolyte (Fig. 5d,e). In addition, the electrodeposited Li morphologies on the LBASEI Li and the pristine Li with E-2 electrolyte are shown in Supplementary Fig. 8. It is important to note that although the above results of the analysis are better with E-1 electrolyte, E-2 electrolyte exhibited more stable performance in the full-cell configuration, which is discussed in next section.

Electrochemical performance of the full cells

The LBASEI Li was used for more in-depth studies in which the anode was paired with a NCM cathode to construct full-cell LiMBs. The LBASEI Li and the NCM cathode were cycled with E-1 electrolyte (Supplementary Fig. 9). Indeed, the LBASEI Li shows better cycling performance than that of with the pristine Li. However, as shown in Fig. 6a, the same cell cycles better with the LBASEI Li with E-2 electrolyte, which contradicts the results obtained from the Li CE and Li migration measurements with asymmetric and symmetric cells. These results imply that developing the LBASEI Li with E-2 electrolyte is more reliable for constructing LiMBs than developing the LBASEI Li with E-1 electrolyte, indicating a high level of importance of the electrolyte choice for developing reliable and electrolyte-compatible ASEIs for real applications of the LBASEI Li anode for LiMBs.

The results reported in Fig. 6a show that cells composed of the LBASEI Li anode and NCM cathode exhibit improved cycling stability (>500 cycles at 1 C) as the anode is stabilized. The cycling performance in Fig. 6a is analysed further by observing the voltage profiles in Fig. 6b,c (Supplementary Note 4). Slow charging and relatively fast discharging processes are desired[32,33] for utilizing the LiM anode in the cell as the LiM anode adopts electroplating mechanisms. Therefore, the LBASEI Li|NCM cell is cycled with E-2 electrolyte at 0.3 C (0.63 mA cm^{-2}) for charging and 1 C for discharging (1.9 mA cm^{-2}), and stable cycling performance is achieved over >1,200 cycles with an initial capacity retention above 80% (Fig. 6d). In the voltage profile (Fig. 6e), the mild potential spike at the beginning of the first charging and leftwards horizontal movement of the traced intersection points are observed, implying that the anode is operating stably over 1,200 cycles and the capacity decrease over the cycles is due to a structural and cathode electrolyte interphase (CEI) degradation of the cathode. To physically observe the surface features of the cycled anode, sliced focused ion beam (FIB) images were taken to analyse the cross-sectional morphologies of the cycled pristine Li (Fig. 6f) and the LBASEI Li (Fig. 6g) anodes from the full cells. For the cycled pristine Li (Fig. 6f), thick, bicontinuous and porous structures are obtained after the cycle. The left and right images are taken at the same position with secondary electron (SE) and backscattered secondary electron (BSE) modes as BSE can provide textural relationships. The pristine Li anode in the BSE mode provides the textural information that the dendrites are porous. Therefore, a large volume expansion as well as dendrite formation severely occurs for the pristine Li anode after the cycles. In Fig. 6g, the cycled LBASEI Li anode shows compact and dendrite-less morphologies. The BSE mode supports that the LBASEI is in its

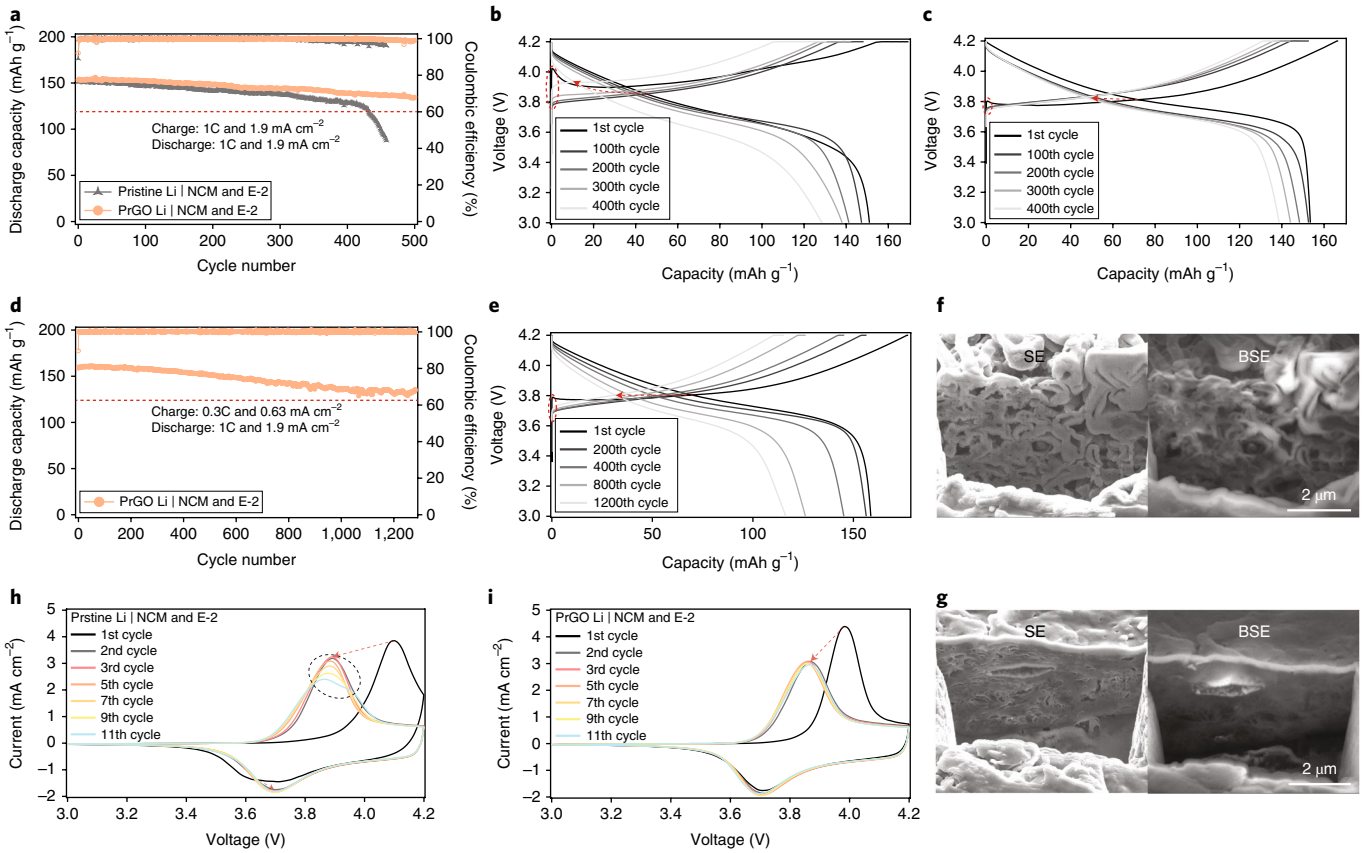

Fig. 6 | Electrochemical performance of the LBASEI Li. a, Cycling profiles of a discharge capacity (filled symbols) and a CE (open symbols) for the pristine Li|NCM and the PrGO Li|NCM full cells at charging/discharging C rates of 1 C/1 C with the operating voltage window of 3.0–4.2 V and E-2 electrolyte. The dashed red horizontal line indicates the capacity limit for 80% of the initial capacity. **b**,**c**, Corresponding voltage profiles of **a** for the pristine Li|NCM cell for 1st–400th cycles (**b**) and the PrGO Li|NCM cell for 1–400th cycles (**c**). The dashed red circles and dashed red arrows indicate the difference of the initial charging potentials from the 1st cycle to the rest of the specified cycles and the trace of the intersection between the charging and discharging potential curves at the specified cycles, respectively. **d**, Cycling profiles of the discharge capacity (filled symbols) and the CE (open symbols) for the PrGO Li|NCM cell at charging/discharging C rates of 0.3 C/1 C with the operating voltage window of 3.0–4.2 V and E-2 electrolyte. The dashed red horizontal line indicates the capacity limit for 80% of the initial capacity. **e**, Corresponding voltage profiles for **d** for the PrGO Li|NCM cell for 1–1,200th cycles. The dashed red circle and dashed red arrow indicate the difference of the initial charging potentials from the 1st cycle to the rest of the specified cycles and the trace of the intersection between the charging and discharging potential curves at the specified cycles, respectively. **f**,**g**, Cross-sectional FIB images of the cycled pristine Li (**f**) and the cycled PrGO Li (**g**) anodes from the full cell taken at SE and BSE modes. **h**,**i**, Cyclic voltammograms of the pristine Li|NCM cell (**h**) and the PrGO Li|NCM cell (**i**) at the scan rate of 0.1 mV s^{-1} with the scanning voltage window of 3.0–4.2 V and E-2 electrolyte. The dashed black circle and dashed red arrows indicate the anodic current responses at the specified cycles and the difference of the anodic and/or cathodic current responses from the 1st cycle to the 2nd cycle, respectively.

intact form with the LBASEI's mechanical stability preserved after the cycles. The electrochemical performance of the LBASEI Li|NCM cells are further investigated and explained (Supplementary Note 5) via cyclic voltammogram analysis as shown in Fig. 6h,i.

Although stable performance of the LBASEI Li with the NCM cathode is verified, the result is still lacking actual practicalities for a real battery system as the above cells were scrutinized with a large excess (~41×) of 380 μm LiM anode with a relatively low areal capacity cathode of 1.9 mAh cm^{-2}. As mentioned previously, utilization of the <30-μm-thick LiM anode[1] and the >4 mAh cm^{-2} cathode[34] is needed to develop practical LiMBs that overcome advancing LiBs. Therefore, a systematically matched capacity of the LBASEI Li anode and high-nickel NCM(811) with an areal capacity of 4.1 mAh cm^{-2} cathode is done to construct more reliable cells. To balance the capacity ratio between negative (anode) and positive (cathode) electrodes in the cell, denoted as the n/p ratio, the n/p ratio ranges from about 1 to 5, meaning that there is 1–5 times the anode capacity than that of the cathode. As 1 mAh cm^{-2} of the Li ideally requires ~4.85-μm-thick LiM, certain LiM thicknesses represent the capacity of the LiM anode, and the n/p ratio can be defined accordingly. Utilizing 20, 50 and 100 μm LiM provides n/p ratios of ~1, ~2.5 and ~5.0, respectively; however, as the NCM cathodes are already lithiated, the n/p ratio can be translated as an additional or excess amount of the LiM anode for LiMBs. In Fig. 7a, the LBASEI on 50 μm LiM anode with the NCM(811) is cycled at charging/discharging rates of 0.3 C/0.5 C followed by one formation cycle at 0.1 C/0.1 C and with E-3 electrolyte, and stable cycle performance, >330 cycles, is achieved with the n/p ratio of ~2.5. E-3 electrolyte is chosen for the thin LiM anodes as it can provide better preservation of the SEIs for the LBASEI than the LBASEI with E-2 electrolyte. To justify, glavanostatic CE profiles are shown in Supplementary Fig. 10, which shows higher CE of the LBASEI Cu|Li cell with E-3 electrolyte than that with E-2 electrolyte. The reason for the improvements can be briefly summarized as E-3 electrolyte having rich fluorine-donating compounds[35,36] with adequate salt[32] and solvent formulations[37] to form stable intrinsic SEIs and CEIs on the electrodes. Moreover, the n/p ratio of ~1, using 20 μm LiM anode, is chosen and cycled with the LBASE Li anode in the full

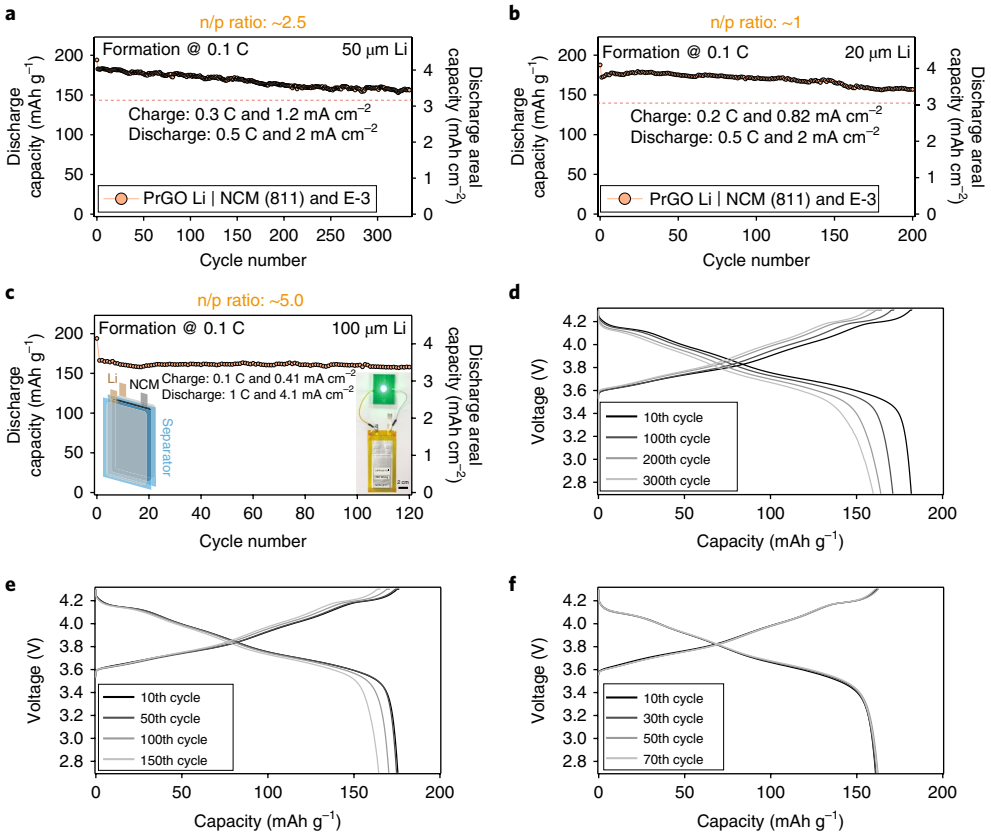

Fig. 7 | Electrochemical performance of the full cell with defined n/p ratios. a, Cycling profiles of a discharge gravimetric capacity (left *y* axis) and a discharge areal capacity (right *y* axis) for the LBASEI on 50 μm Li with NCM(811) cell, PrGO Li|NCM(811), at charging/discharging C rates of 0.3 C/0.5 C with a operating voltage window of 2.7–4.3 V and E-3 electrolyte. The dashed red horizontal line indicates the capacity limit for 80% of the initial capacity. **b**, Cycling profiles of the discharge gravimetric capacity (left *y* axis) and the discharge areal capacity (right *y* axis) for the LBASEI on 20 μm Li with NCM(811) cell, PrGO Li|NCM(811), at charging/discharging C rates of 0.2 C/0.5 C with an operating voltage window of 2.7–4.3 V and E-3 electrolyte. The dashed red horizontal line indicates the capacity limit for 80% of the initial capacity. **c**, Cycling profiles of the discharge gravimetric capacity (left *y* axis) and the discharge areal capacity (right *y* axis) for the LBASEI on 100 μm-Li with NCM(811) pouch-format battery at charging/discharging C rates of 0.1 C/1 C with the operating voltage window of 2.7 V–4.3 V and E-3 electrolyte. The insets show stacking configuration (left) and fabricated LiMB (right). The pouch battery can light a green LED as the threshold voltage of the green LED is up to 4 V. **d**–**f**, Corresponding voltage profiles of the LBASEI on 50 μm Li with NCM(811) cell for 10th–300th cycles (**d**), the LBASEI on 20 μm Li with NCM(811) cell for 10th–150th cycles (**e**) and the LBASEI on 100 μm Li with NCM(811) pouch battery for 10th–70th cycles (**f**).

cell as well (Fig. 7b) at charging/discharging rates of 0.2 C/0.5 C. More than 200 cycles are achieved, indicating promising cycling performance for constructing practical LiMBs. The electrochemical effect of the n/p ratio is explained in detail in Supplementary Note 6. Moreover, 260 Wh kg^{-1} (incorporating the weight of all cell components, except for the sealants and tabs), pouch-format batteries are constructed with the LBASEI Li (100 μm LiM) anode and NCM(811) cathode, and more than 120 cycles of stable cycling performance are demonstrated (Fig. 7c). To understand the stable cycling of the cells in Fig. 7a–c, corresponding voltage profiles are observed (see Fig. 7d–f). All exhibit stable voltage profile trends where the charge/discharge intersection points from the curves slighlty move horizontally leftward or remain almost constant, a good indication of the stable electrochemical performance of the LBASEI Li anode in the pouch-format LiMBs.

Conclusions

We have designed a phosphate-functionalized graphene oxide LBASEI for the LiM anode that physicochemically stabilizes Li migration by favoured interaction of the Li with pyro-/metaphosphates and phosphorus species present in the LBASEI. Also, the thickness optimization of the LBASEI is performed by nucleation overpotential analysis. Further effort was taken to utilize the developed LBASEI for various thicknesses of commercially available LiM anodes. Moreover, utilizing the compatible electrolyte system for the LBASEI and for the full cells and balancing the electrodes' capacity ratios, the n/p ratios, for the LiMBs are demonstrated. For the result, the LBASEI on the 20 μm Li anode, with areal capacity of ~4.12 mAh cm^{-2}, and the NCM(811) cathode, with areal capacity of 4.1 mAh cm^{-2}, are paired to construct the full cell with n/p ratio of ~1, and >200 cycles are achieved. In addition, the 260 Wh kg^{-1} pouch LiMB was fabricated and analysed, which stably performs >120 cycles. These prospective results could allow facile and practical creation of diverse ranges and types of ASEIs on commercially available LiM anodes to construct reliable LiMBs with contemporary selections of cathodes that could outperform conventional and advancing LiBs. It should be noted that further efforts are needed to enable long-term cycling of the LiMBs that utilize the thin LiM anode at high charging rates.

Methods

Graphene synthesis. The rGO, PrGO and NrGO used in the study are synthesized as follows. For rGO, graphene oxide was synthesized via a modified Hummer's method[38,39], and graphite flakes (Sigma Aldrich) were dispersed in concentrated

sulfuric acid (Sigma Aldrich) and cooled to 0 °C. Potassium permanganate (Sigma Aldrich) solution was then added dropwise at a temperature of <10 °C. After, distilled water and hydrogen peroxide were added to the solution. The graphene oxides are then collected by filtrating the suspension with deionized water. The synthesized graphene oxides were reduced under ambient pressure with hydrogen gas (flow rate of 100 sccm) at 800 °C for 150 min. For PrGO, 1 ml of concentrated phosphoric acid (>84 wt% in H_2O, Sigma Aldrich) and 200 mg of synthesized rGO were mixed first then pyrolyzed under ambient pressure with Ar gas (flow rate of 500 sccm) at 800 °C for 2 h. For NrGO, the synthesized graphene oxides were reduced under ambient pressure with NH_3 gas (flow rate of 100 sccm) at 800 °C for 2 h. All the graphene oxides used in the study were first cooled to room temperature after the reactions and cleaned with deionized water and ethanol. The cleaned graphene oxides were stored as concentrated graphene suspensions with pure ethanol.

LBASEI preparation. Suspensions of rGO, PrGO and NrGO were made by dispersing the respective graphene oxides (1–3 wt%) in pure ethanol, followed by sonication for 30–50 min to disperse the graphene oxides. Desired thicknesses of the LBASEI were created on Cu foil via the LBS method[28,29]. Briefly, the Cu foil was cut to 6 cm × 10 cm. Then, the foil was submerged in a water-filled beaker, and the desired graphene oxide suspension was constantly injected at the water surface to fabricate the LBASEI. By simultaneously raising the submerged Cu when about 30–50% of the water surface was covered by the self-assembled LB film, the LBASEI was continuously deposited after obtaining the desired thickness by repeating the LBS process. The graphene LBASEI-coated Cu was then finally dried on a hot plate at 110 °C for 1 min and in a vacuum oven at 50 °C overnight. The thickness of the LBASEI was measured via a LEXT OLS4100 (Olympus) microscope using a three-dimensional mapping tool. A video demonstration of the LBASEI preparation is provided in Supplementary Video 1. The video shows the LBASEI fabrication process on a B5-sized aluminium substrate supported with a polycarbonate sheet to reveal adaptability of the large-scale processing. A concentrated graphene nanoplatelet (DT-GR-M05, Dittotechnology) suspension, ~5 wt% in pure ethanol, was used for this demonstration for clear visibility of the LBASEI.

LBASEI Li anode fabrication. The LBASEI film was transferred onto the desired thickness of lithium foil via the roll-press process. Under dry atmospheric conditions (dew point <−60 °C), a stacking configuration of Mylar-film|Cu|lithium|LBASEI|Cu|Mylar-film was applied and all were sandwiched together at first. Then the stacked components were uniformly pressed using the roll-press with a cylinder distance of 70–80% of the total thickness of the stacked components with a rolling speed of 0.5 cm s^{-1}. After the roll-press, Mylar-films were removed and the Cu foil was peeled-off. The transfer process in action and details are provided in Supplementary Video 2. The LBASEI Li electrode was cut into circular disks with diameter of 1.5 cm for the coin cell (CR2032) measurements and was cut into 4 cm × 6 cm for the pouch battery fabrications.

Density functional theory calculations. First-principles electronic structure calculations were performed using density functional theory as implemented in VASP (VASP 5.3)[40]. Generalized gradient approximation proposed by Perdew, Burke and Ernzerhof was employed to understand the electron correlation[41,42]. For the estimation of electron–ion interactions, projected augmented wave formalism was used. All the atoms were relaxed until the force on each atom was ≤0.001 eV A^{-1}. An energy cut-off of 500 eV was used to restrict the plane-wave basis set. A vacuum layer of 15 Å was used to avoid the interlayer interactions. To mimic the graphene model containing P or N derivative functional groups, zigzag nanoribbons were considered with width of ~10 Å passivated with hydrogen atoms[43,44]. K-space sampling of the first Brillouin zone was performed using a Monkhorst–Pack k-space mesh of 25 × 1 × 1 (ref. [45]). Van-der Waals interactions were incorporated to consider the long-range interactions between the Li atoms and the various functional species on the graphene substrate using vDW-DF function[46]. The binding energies were calculated by subtracting $E_{substrate}$ and E_{Li} from E_{total}, where E_{total} is the energy of the substrate after the lithiation, and $E_{substrate}$ and E_{Li} are the energy of the graphene containing various species and the Li atoms, respectively. The energy of the Li atom was calculated using the metallic Li configuration. Negative binding energy values correspond to the bound state having attractive interactions of the Li with the substrate. Two-dimensional local charge density profiles were also analysed to understand the localization of charge caused by the presence of the functional groups.

Electrochemical measurements. Three different types of the electrolytes, denoted as E-1, E-2 and E-3, were used in this study. The formulations of the indicated electrolytes are provided accordingly. E-1: 0.5 M lithium bis(trifluoromethanesulfonyl)imide (LiTFSI, Sigma Aldrich) and 0.5 M lithium bis(fluorosulfonyl)imide (LiFSI, Lichem) in fluoroethylene carbonate (FEC, PanaX Etech):dimethyl carbonate (DMC, PanaX Etech) by 3:7 volume ratio. E-2: 0.6 M LiTFSI, 0.4 M lithium bis-(oxalato)borate (LiBOB, Sigma Aldrich), and 0.05 M lithium hexafluorophosphate ($LiPF_6$, PanaX Etech) in ethylene carbonate (EC, PanaX Etech):DMC by 1:1 volume ratio with 1 wt% FEC and 2 wt% vinylene carbonate (VC, PanaX Etech). E-3: 0.6 M LiTFSI, 0.4 M LiBOB, 0.4 M lithium fluoride (LiF, Sigma Aldrich), 0.1 M lithium nitrate ($LiNO_3$, Junsei Chemical), 0.05 M $LiPF_6$ and 0.03 M lithium tetrafluoroborate ($LiBF_4$, Sigma Aldrich) in EC:DMC by 2:1 volume ratio with 1 wt% FEC and 2 wt% VC and 3 wt% di-2,2,2-trifluoroethyl carbonate (TFEC, TCI Tokyo Chemical). The above electrolytes were used as indicated in the manuscript. The salts were fully dissolved into the solvent first (24–72 h stirring and sonicating ~20 min afterwards in an inert environment), then the solvent additives were added accordingly. All electrolytes were made and cells were measured at 25–28 °C.

For the nucleation overpotential analysis, asymmetric Li coin cells were fabricated. An 11-μm-thick polyethylene (W-Scope Korea) separator was used for all the coin cells and the pouch LiMBs. For the Cu electrode, pristine Cu and ~1-μm-thick each of PrGO-, NrGO- or rGO-coated Cu (1.5 cm in diameter) disks were used as the reference electrode whereas the counterelectrode was 380-μm-thick LiM (1.5 cm in diameter) with the same LBASEI coatings applied and with 30 μl E-2. A galvanostatic potentiostat (Biologics VSP/VMP3) was used to obtain voltage profiles for the nucleation overpotential with areal current density of 0.05 mA cm^{-2}. The 0- to ~3-μm-thick PrGO LBASEI on Cu was prepared via the LBS method and tested with the same conditions above.

The asymmetric coin cells were used to measure the CE from the LBASEI Cu and the LBASEI Li electrodes. For the electrodes, 2–3-μm-thick PrGO-coated Cu and 380-μm-thick LiM (1.5 cm in diameter) with the same LBASEI coating applied were used with 30 μl E-1. Current density and capacity of 1 or 3 mA cm^{-2} and 1 or 3 mAh cm^{-2}, respectively, were used. For the Li migration measurements, same as the Li plating/stripping, galvanostatic current was applied. Accordingly, 1 or 3 mA cm^{-2} was applied for 1 h for the Li plating, and the same areal current density was applied for the Li stripping with the voltage cut-off at 2 V.

The symmetric Li coin cells with and without the 2–3 μm LBASEI on the LiM (1.5 cm diameter) disks were used as the electrodes with the 11 μm separator and 30 μl of E-1 and E-2 electrolytes for a.c. impedance spectroscopy and the Li migration measurements. For the a.c. impedance spectroscopy (Biologics VSP/VMP3) measurements, a frequency range of 1 MHz–0.5 Hz was used. For the Li migration measurement, galvanostatic current with areal current density and capacity of 1 mA cm^{-2} and 1 mAh cm^{-2}, respectively, were used.

Cathodes (1.2-cm-diameter disk) of 1.9 mAh cm^{-2} NCM ($LiNi_{0.6}Co_{0.2}Mn_{0.2}O_2$, supplied by Kokam) and 4.1 mAh cm^{-2} NCM(811) ($LiNi_{0.8}Co_{0.1}Mn_{0.1}O_2$, supplied by LG Chem) were used for constructing full-cell configured coin cells. Various thicknesses, 20, 50, 100 and 380 μm, of the LiM (Honzo metal Japan supplied by KISCO Korea) with the 2–3 μm LBASEI were used with the 11 μm separator (1.8-cm-diameter disk) and 30 μl of E-1, E-2 and E-3 electrolytes, as indicated in the manuscript. For the constant voltage during the galvanostatic charging, the cut-off current value was set as 0.05 C. The voltage windows for the cells with NCM and NCM(811) cathodes were set to 3.0–4.2 V and 2.7–4.3 V, respectively. The operating voltage window difference was set to fully utilize the cathode for NCM(811) to maximize the capacity and the operating voltage window. For constructing the pouch LiMBs, two 4 cm × 6 cm-sized 10-μm-thick Cu|102–103-μm-thick LBASEI Li and one 4 cm × 6 cm-sized double-sided NCM(811), NCM(811)|8-μm-thick Al|NCM(811), cathode were used as the electrodes with two 5 cm × 7 cm separators and 300 μl of E-3 electrolyte (see the inset of Fig. 7c for the cell configuration). All cell fabrications were done in a dry capsule under the dew point of <−60 °C. The operating voltage window was set to 2.7–4.3 V. For the constant voltage during the galvanostatic charging, the cut-off current value was set to 0.05 C. One formation cycle at 0.1 C charging/discharging was performed, and the following cycles were performed with 0.1 C charging and 1 C discharging. The cycling performance of all the cells and LiMBs were analysed by Maccor battery cyclers.

Characterization. The XPS (PHI 5000 VersaProbe-Ulvac-PHI) measurements were performed on each of rGO, NrGO and PrGO to investigate the surface features of the binding species. Each of the graphene oxides were placed on a holder and measured with a background pressure of 2.0×10^{-1} Pa, source of Monochromator Al Ka (1486.6 eV) anode (24.5 W, 15 kV), spot size of 100 μm × 100 μm and calibrating C 1s peak (284.6 eV). Electrode morphologies were investigated via scanning electron microscopy (Teneo Volume Scope SEM) and FIB microscopy (Quanta 3D FEG FEI). The cycled cells were opened in a glove box (Korea Kiyon), and the cycled anodes were fully cleaned by washing the anode with DMC solvent and drying in a vacuum oven. To avoid electrode contaminations and side reactions, all of the Li samples were transported from the glove box to the FIB instruments in a sealed container protected by Ar gas. For obtaining FIB images on the cycled Li, accelerating voltages of 5 kV and 14 kV were used for the SE and BSE modes, respectively. For a milling of the LBASEI Li and the pristine Li anodes, first Pt deposition condition of electron beam (5 kV, 0.38 nA) and ion beam (30 kV, 0.1 nA) was applied, and the ion beam milling (accelerating voltage 30 kV, and beam current 7 nA (rough milling) and 0.5 nA (fine milling)) was performed on the targeted area of the anodes.

Data availability

The data that support the plots within this paper and other findings of this study are available from the corresponding authors upon reasonable request.

Received: 15 April 2018; Accepted: 7 August 2018;
Published online: 24 September 2018

References

1. Albertus, P., Babinec, S., Litzelman, S. & Newman, A. Status and challenges in enabling the lithium metal electrode for high-energy and low-cost rechargeable batteries. *Nat. Energy* **3**, 16–21 (2018).
2. Cheng, X. B., Zhang, R., Zhao, C. Z. & Zhang, Q. Toward safe lithium metal anode in rechargeable batteries: a review. *Chem. Rev.* **117**, 10403–10473 (2017).
3. Larcher, D. & Tarascon, J.-M. Towards greener and more sustainable batteries for electrical energy storage. *Nat. Chem.* **7**, 19–29 (2015).
4. Armand, M. & Tarascon, J.-M. Building better batteries. *Nature* **451**, 652–657 (2008).
5. Goodenough, J. B. & Kim, Y. Challenges for rechargeable Li batteries. *Chem. Mater.* **22**, 587–603 (2010).
6. Wei, S., Choudhury, S., Tu, Z., Zhang, K. & Archer, L. A. Electrochemical interphases for high-energy storage using reactive metal anodes. *Acc. Chem. Res.* **51**, 80–88 (2018).
7. Liang, X. et al. A facile surface chemistry route to a stabilized lithium metal anode. *Nat. Energy* **6**, 17119 (2017).
8. Tu, Z. et al. Fast ion transport at solid–solid interfaces in hybrid battery anodes. *Nat. Energy* **3**, 310–316 (2018).
9. Choudhury, S. et al. Designer interphases for the lithium-oxygen electrochemical cell. *Sci. Adv.* **3**, 1602809 (2017).
10. Lin, D., Liu, Y. & Cui, Y. Reviving the lithium metal anode for high-energy batteries. *Nat. Nanotech.* **12**, 194–206 (2017).
11. Tikekar, M. D., Choudhury, S., Tu, Z. & Archer, L. A. Design principles for electrolytes and interfaces for stable lithium-metal batteries. *Nat. Energy* **1**, 1–7 (2016).
12. Tikekar, M. D., Archer, L. A. & Koch, D. L. Stabilizing electrodeposition in elastic solid electrolytes containing immobilized anions. *Sci. Adv.* **2**, 1600320 (2016).
13. Tu, Z. et al. Designing artificial solid-electrolyte interphases for single-ion and high-efficiency transport in batteries. *Joule* **1**, 394–406 (2017).
14. Guo, Y., Li, H. & Zhai, T. Reviving lithium-metal anodes for next-generation high-energy batteries. *Adv. Mater.* **29**, 1–25 (2017).
15. Kim, M. S. et al. Designing solid-electrolyte interphases for lithium sulfur electrodes using ionic shields. *Nano Energy* **41**, 573–582 (2017).
16. Lin, D. et al. Layered reduced graphene oxide with nanoscale interlayer gaps as a stable host for lithium metal anodes. *Nat. Nanotech.* **11**, 626–632 (2016).
17. Liu, S. et al. Crumpled graphene balls stabilized dendrite-free lithium metal anodes. *Joule* **2**, 184–193 (2018).
18. Liu, L. et al. Free-standing hollow carbon fibers as high-capacity containers for stable lithium metal anodes. *Joule* **1**, 563–575 (2017).
19. Yan, K. et al. Selective deposition and stable encapsulation of lithium through heterogeneous seeded growth. *Nat. Energy* **1**, 16010 (2016).
20. Liu, L. et al. Uniform lithium nucleation/growth induced by lightweight nitrogen-doped graphitic carbon foams for high-performance lithium metal anodes. *Adv. Mater.* **30**, 1706216 (2018).
21. Deng, W., Zhou, X., Fang, Q. & Liu, Z. Microscale lithium metal stored inside cellular graphene scaffold toward advanced metallic lithium anodes. *Adv. Energy Mater.* **8**, 1703152 (2018).
22. Zhang, R. et al. Lithiophilic sites in doped graphene guide uniform lithium nucleation for dendrite-free lithium metal anodes. *Angew. Chem. Int. Ed.* **56**, 7764–7768 (2017).
23. Raji, A. O. et al. Lithium batteries with nearly maximum metal storage. *ACS Nano* **11**, 6362–6369 (2017).
24. Lin, D. et al. Layered reduced graphene oxide with nanoscale interlayer gaps as a stable host for lithium metal anodes. *Nat Nano* **11**, 626–632 (2016).
25. Liang, Z. et al. Composite lithium metal anode by melt infusion of lithium into a 3D conducting scaffold with lithiophilic coating. *Proc. Natl Acad. Sci. USA* **113**, 2862–2867 (2016).
26. Liu, Y. et al. Lithium-coated polymeric matrix as a minimum volume-change and dendrite-free lithium metal anode. *Nat. Commun.* **7**, 10992 (2016).
27. Zhi, J., Zehtab Yazdi, A., Valappil, G., Haime, J. & Chen, P. Artificial solid electrolyte interphase for aqueous lithium energy storage systems. *Sci. Adv.* **3**, 1701010 (2017).
28. Kim, M. S., Choudhury, S., Moganty, S. S., Wei, S. & Archer, L. A. Fabricating multifunctional nanoparticle membranes by a fast layer-by-layer Langmuir–Blodgett process: application in lithium–sulfur batteries. *J. Mater. Chem. A* **4**, 14709–14719 (2016).
29. Kim, M. S., Ma, L., Choudhury, S. & Archer, L. A. Multifunctional separator coatings for high-performance lithium–sulfur batteries. *Adv. Mater. Interfaces* **3**, 1600450 (2016).
30. Kresse, G. & Furthmu, J. Efficient iterative schemes for ab initio total-energy calculations using a plane-wave basis set. *Phys. Rev. B* **54**, 11169 (1996).
31. Adams, B. D., Zheng, J., Ren, X., Xu, W. & Zhang, J. G. Accurate determination of coulombic efficiency for lithium metal anodes and lithium metal batteries. *Adv. Energy Mater.* **8**, 1702097 (2017).
32. Zheng, J. et al. Electrolyte additive enabled fast charging and stable cycling lithium metal batteries. *Nat. Energy* **2**, 17012 (2017).
33. Qian, J. et al. Anode-free rechargeable lithium metal batteries. *Adv. Funct. Mater.* **26**, 7094–7102 (2016).
34. Jiao, S. et al. Behavior of lithium metal anodes under various capacity utilization and high current density in lithium metal batteries. *Joule* **2**, 110–124 (2018).
35. Suo, L. et al. Fluorine-donating electrolytes enable highly reversible 5-V-class Li metal batteries. *Proc. Natl Acad. Sci. USA* **115**, 1156–1161 (2018).
36. Fan, X. et al. Non-flammable electrolyte enables Li-metal batteries with aggressive cathode chemistries. *Nat. Nanotech.* **13**, 715–722 (2018).
37. Li, X. et al. Dendrite-free and performance-enhanced lithium metal batteries through optimizing solvent compositions and adding combinational additives. *Adv. Energy Mater.* **8**, 1703022 (2018).
38. Kovtyukhova, N. I. et al. Layer-by-layer assembly of ultrathin composite films from micron-sized graphite oxide sheets and polycations. *Chem. Mater.* **11**, 771–778 (1999).
39. Hummers, W. S. & Offeman, R. E. Preparation of graphitic oxide. *J. Am. Chem. Soc.* **80**, 1339–1339 (1958).
40. Kresse, G. & Hafner, J. Norm-conserving and ultrasoft pseudopotentials for first-row and transition elements. *J. Phys. Condens. Matter.* **6**, 8245–8257 (1994).
41. Perdew, J. P., Burke, K. & Ernzerhof, M. Generalized gradient approximation made simple. *Phys. Rev. Lett.* **77**, 3865–3868 (1996).
42. Perdew, J. P. & Wang, Y. Accurate and simple analytic representation of the electron-gas correlation energy. *Phys. Rev. B* **45**, 244–249 (1992).
43. Deepika, Kumar, S., Shukla, A. & Kumar, R. Origin of multiple band gap values in single width nanoribbons. *Sci. Rep.* **6**, 36168 (2016).
44. Deepika, Kumar, T. J. D., Shukla, A. & Kumar, R. Edge configurational effect on band gaps in graphene nanoribbons. *Phys. Rev. B* **91**, 1–5 (2015).
45. Pack, J. D. & Monkhorst, H. J. Special points for Brillouin-zone integrations. *Phys. Rev. B* **16**, 1748–1749 (1977).
46. Klimeš, J., Bowler, D. R. & Michaelides, A. Chemical accuracy for the van der Waals density functional. *J. Phys. Condens. Matter.* **22**, 246401 (2010).

Acknowledgements

This work was supported by the National Research Foundation of Korea (NRF-2016M1B3A1A01937324) and the Korea Institute of Science and Technology (KIST) Institutional Program (Project No. 2E28141). L.A.A. also acknowledges support from the US Advanced Research Projects Agency — Energy (ARPA-E) through award #DE-AR0000750. D. thanks Virtual lab www.vfab.org for the Cloud Computing Interface and the KIST supercomputing facility.

Author contributions

M.S.K., L.A.A. and W.I.C. designed and conceptualized the study. J.-H.R. prepared Langmuir–Blodgett artificial SEIs on specified substrates and provided technical support. D. performed density functional theory calculations for the Li atom binding energies and the charge density analysis on the specified species and atomic structures. Y.R.L. and I.W.N. prepared graphene oxides and helped with XPS experiments. K.-R.L supervised the computational study. W.I.C and L.A.A supervised the overall study. M.S.K performed all the experiments, characterization and analysis and wrote the manuscript. All the authors discussed the manuscript and provided comments.

Competing interests

The authors declare no competing interests.

Additional information

Supplementary information is available for this paper at https://doi.org/10.1038/s41560-018-0237-6.

Reprints and permissions information is available at www.nature.com/reprints.

Correspondence and requests for materials should be addressed to L.A.A. or W.C.

Publisher's note: Springer Nature remains neutral with regard to jurisdictional claims in published maps and institutional affiliations.